Transmission of OFDM-UWB radio signals along multimode fiber in in-building networks

Filipa Andreia Fernandes Henriques

Instituto Superior Técnico/Instituto de Telecomunicações
Av. Rovisco Pais, Lisbon, Portugal
filipafhenriques@gmail.com

***Abstract*—Nowadays, in-building networks are facing a new challenge of upgrading their capacity to exceeding 1 Gbit/s, in order to provide high definition television (HDTV) and new advanced multimedia-based applications requiring even higher capacity than HDTV. The main characteristics of multimode fibers (MMF) like the low cost and their efficiency in short-range links make these fibers adequate to be used in in-building networks. The main features of orthogonal frequency division multiplexing (OFDM) ultra-wideband (UWB) signals like the low inter-symbol interference (ISI) and the tolerance to multipath fading, make these signals appropriate to be used in MMF systems. In this dissertation, the transmission of OFDM-UWB radio signals along multimode fibers in in-building networks is analysed. A numerical model of the fiber modal dispersion is developed in MATLAB. The transmission performance of the OFDM-UWB signals along the MMF is evaluated using the semi-analytical Gaussian approach and the maximum distance for single and multi-band transmission is assessed. The numerical results show that the maximum transmission distance is very dependent on the power launching conditions, on the fiber length and on the number of sub-bands used. The maximum assessed distance ranges from 560 m (achieved for single-band transmission and for centred launching conditions) to less than 50 m (achieved for simultaneous transmission of 3 OFDM-UWB sub-bands and for centred launching conditions).**

***Index Terms*—Multimode optical fiber, OFDM-UWB signals, modal dispersion, launching conditions, in-building networks.**

I. Introduction

Ultra wide band (UWB) technology is being widely recognised due to its main features like low self-interference, tolerance to multipath fading and low probability of interception[1]. UWB is a radio modulation technique with 500 MHz minimum bandwidth or, at least, 20% greater than the centre frequency operation [2]. There are two UWB signal formats: Impulse Radio (IR) and orthogonal frequency division multiplexing ultra wide band (OFDM-UWB) [3]. In this work, it is used the OFDM-UWB format, since it presents a better performance for high bit rates [4]. Some of the benefits of using OFDM modulation are high-spectral efficiency, resiliency to radio frequency (RF) interference and lower multipath distortion [5]. The enhanced features of the multimode fiber (MMF) in short ranges links make them adequate to be used in in-building networks. In this paper, we study and characterize the OFDM-UWB radio signals, in the time and frequency domain, along multimode fiber propagation. Based on the modal theory, a numerical model is developed. This model allows to study the impact of the fiber transmission and the power launching conditions on the performance of the system, by evaluating the degradation of the quality of the received signal and the bit error probability and assess the maximum transmission distance in single- and multi-channel OFDM-UWB systems. This paper is structured as follows. In Section II, the description of the OFDM-UWB transmission system over the multimode fiber is presented and analysed. In Section III, the multimode fiber propagation model is presented and discussed. In Section IV, the performance results of the whole OFDM-UWB multimode fiber system are presented and discussed. In Section V, the conclusions of this dissertation and the future work to be done about this subject are presented.

II. OFDM-UWB system description and analysis

A. OFDM-UWB system description

In Figure 1, the block diagram of the OFDM-UWB system used in this work is presented.

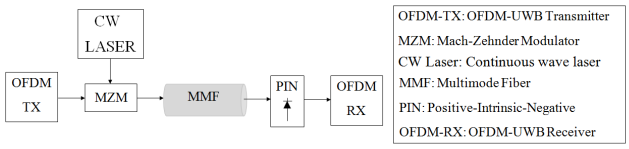

Fig. 1: Representative scheme of the OFDM-UWB system used in this work.

The first element of the OFDM-UWB system is the transmitter, where the OFD-UWB signals are generated. Once these signals are built, the next step is to do the electro-optic conversion through the Mach-Zehnder modulator, which allows the signal to be transmitted over the multimode optical fiber. At the fiber's output, the signal is converted from optic to electric by the Positive-Intrinsic-Negative (PIN), and it is ready to be processed by the OFDM-UWB receiver. The main components of this system are presented with more detail in the following sections.

1) OFDM-UWB signals: The OFDM-UWB approach divides the UWB spectrum (3.1 to 10.6 GHz) into 14 sub-bands, each with 528 MHz wide [4]. The center frequency of OFDM-UWB signal in each 528-MHz band is given by:

$$f_c = 2904 + 528 n_b, \quad [MHz] \quad n_b = 1, 2, \ldots, 14 \tag{1}$$

where n_b is the number of the sub-band used.

The bit rate of the system is given by [6]:

$$R_b = \frac{N_{sc}}{T_s} \log_2 M \tag{2}$$

So, for N_{sc}=100, T_s=312.5 ns and M=4 (since it is being used Quadrature Phase Shift Keying (QPSK) modulation), the system presents a bit rate of 640 Mbit/s.

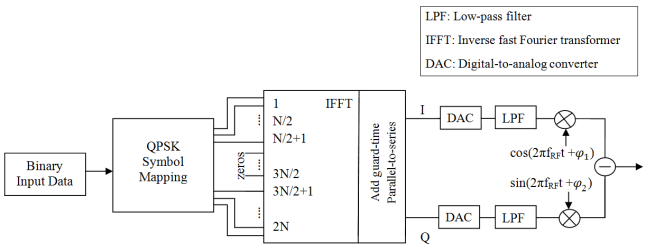

Fig. 2: Block diagram of the OFDM-UWB transmission system.

2) OFDM-UWB transmitter: A block diagram of the OFDM-UWB transmitter is presented in Figure 2.

An input binary deBruijn sequence with 2^{13} symbols is converted into a complex-valued sequence using QPSK modulation. After that, the complex-valued signal is converted from series to parallel and an inverse fast Fourier transform (IFFT) is applied. The transmitted signal is now splitted in an in-phase (I) component and in a quadrature (Q) component, which contains the real and the imaginary values of the original signal, respectively. These components are first converted to the analogue domain using digital-to-analogue (DAC) converters. The analogue signals are then used to modulate cosine and sine waves at the carrier frequency, respectively. A low pass filter (LPF) is now applied to each component, in order to reduce the influence of the aliasing components on the system performance [7]. After that, the I and Q components are up-converted to the carrier frequency of the UWB sub-band used. At the OFDM-UWB transmitter, 32 OFDM-UWB symbols are generated.

3) OFDM-UWB receiver: A representative scheme of the OFDM-UWB receiver is presented in Figure 3.

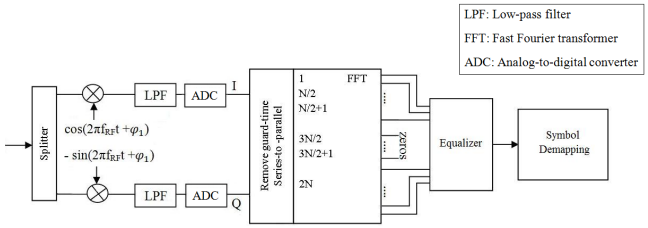

Fig. 3: Block diagram of the OFDM-UWB receiver.

At the OFDM-UWB receiver firstly, the transmitted signal is splitted in two components: an in-phase component, which leads to the real values of the original signal and a quadrature component, which leads to the imaginary values of the original signal. After this, each of these signals is down-converted and filtered. The baseband signals are then sampled and digitised using analogue-to-digital (ADC) converters. The guard-time of the OFDM-UWB signals is removed and the signals are converted from series to parallel. Then, a fast Fourier transform (FFT) is applied to the resulting waveform and the equalizer transfer function is estimated from the pilot subcarrier information. The pilots information is used to compensate for the amplitude and phase distortions induced on the signal along the transmission system [7], by providing a polynomial interpolation of the channel between the pilots. The final step is to do the symbol demapping and the received constellation is obtained.

4) Electrical noise: The PIN performs the opto-electric conversion of the received signal. First, the signal is photodetected and then is pre-amplified and filtered, before it reaches the OFDM-UWB receiver. A simplified scheme of the system PIN + pre-amplifier is presented in Figure 4.

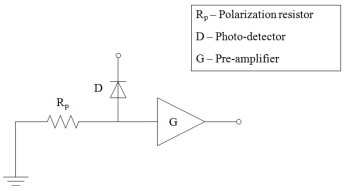

Fig. 4: Block diagram of the system PIN + pre-amplifier.

The polarization resistor and the pre-amplifier introduce electrical noise into the system, due to the existence of resistive and active elements on them, respectively. This electric noise is also known as circuit noise and is represented by σ_c^2. The noise associated with the polarization resistor R_p, can be determined by the current variance associated with it [8]:

$$\sigma_b^2 = \frac{4k_BT}{R_p}B_{e,n} \tag{3}$$

where k_B is the Boltzman constant, T is the temperature (in Kelvin), R_p is the polarization resistor at the pre-amplifier input and $B_{e,n}$ is the equivalent bandwidth of the electric noise. The pre-amplifier noise can be described by its noise figure, $f_{n,e}$. So, the total noise circuit of the system is given by the contributions of the resistive noise and of the amplifier noise figure:

$$\sigma_c^2 = \sigma_b^2 \cdot f_{n,e} = \frac{4k_BT}{R_p} \cdot f_{n,e} \cdot B_{e,n} \tag{4}$$

Finally, from the analysis of the Equation 4 ,it is possible to determine the power spectral density (PSD) of the circuit noise, once $B_{e,n}$ is the equivalent bandwidth of the electric noise:

$$S_c(f) = \frac{\sigma_c^2}{B_{e,n}} = \frac{4k_BT}{R_p}f_{n,e} \tag{5}$$

Table I shows the numerical values used for the circuit noise of the OFDM-UWB system.

TABLE I: Parameters used for the electrical noise.

Parameters	
Boltzman constant	$k_B = 1.38 \times 10^{-23}$ J/K
Polarization resistor	$R_p = 50\ \Omega$
Temperature	$T = 290$ K
Noise figure	$f_{n,e} = 10$
Electrical PSD noise	
$S_c(f) = 3.2 \times 10^{-21}$ A^2/Hz	

B. Back-to-back system results

In order to study the OFDM-UWB system performance, firstly the back-to-back configuration (with no fiber transmission), shown in Figure 5, is analysed. The bit error ratio (BER) of the system is determined by using the semi-analytic gaussian approach presented in [9].

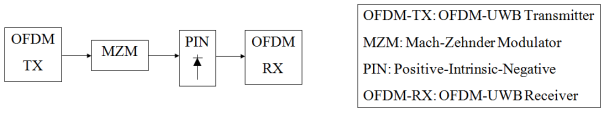

Fig. 5: Block diagram of the OFDM-UWB system in *back-to-back* configuration.

The performance analyse of the block diagram represented in Figure 5 allows studying how the transmitted signal is affected by the different components of the system, without taking into account the multimode fiber propagation effect. This study allows verifying the reliability of the transmission system. In the following sections, the results for single- and multi-band transmission are presented.

C. Single-channel transmission

Figure 6 and Figure 7 show the received constellations without noise at the OFDM-UWB receiver output in back-to-back configuration, for the first four UWB sub-bands.

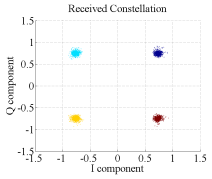

(a) First UWB sub-band.

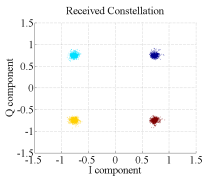

(b) Second UWB sub-band.

Fig. 6: Received constellations for the first and the second UWB sub-bands.

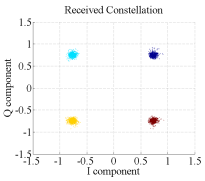

(a) Third UWB sub-band.

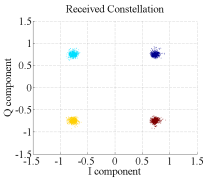

(b) Fourth UWB sub-band.

Fig. 7: Received constellations for the third and the fourth UWB sub-bands.

The results presented in Figure 6 and in Figure 7 show that the received constellations for the first four UWB sub-bands are identical, although they are not equals to the sent one. This result is expected since the system components are not ideals. The Bessel filters, the up and down-converting processes, the photo-detection and the pre-amplification processes introduce some distortion into the signal, originating the non-ideal constellations presented in Figure 6 and in Figure 7. Nevertheless, the received constellations are very good: they are concentrated in a small area and they are perfectly apart from each other. This happens because the signal does not suffers any significant loss nor distortion for these sub-bands, which means that all the bits are correctly demapped.

D. Multi-channel transmission

Figure 8, Figure 9 and Figure 10 show the received constellations without noise at the OFDM-UWB receiver output in back-to-back configuration, when more than one sub-band is used simultaneously. For the multi-band situation, it is assumed that the performance of the system is given by the performance of the worst sub-band.

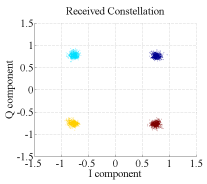

(a) First OFDM-UWB sub-band.

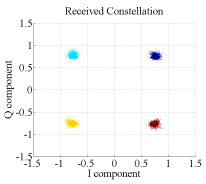

(b) Second OFDM-UWB sub-band.

Fig. 8: Received constellations for simultaneous transmission of the first two OFDM-UWB sub-bands.

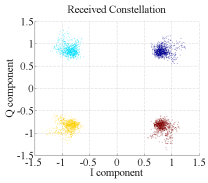

(a) First OFDM-UWB sub-band.

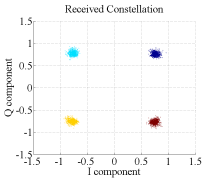

(b) Second OFDM-UWB sub-band.

Fig. 9: Received constellations of the first and the second OFDM-UWB sub-band for simultaneous transmission of the first three OFDM-UWB sub-bands.

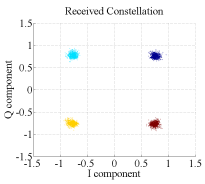

Fig. 10: Received constellation of the third OFDM-UWB sub-band for simultaneous transmission of the first three OFDM-UWB sub-bands.

Figure 9 and Figure 10 show that the performance of the system for simultaneous transmission of the first three UWB sub-bands is limited by the performance of the first UWB sub-band, which presents a significant distortion when compared with the other two sub-bands used in this multi-band transmission. So, the use of more than two sub-bands simultaneously leads to the increase of the distortion of the received signal. One justification of this effect is the interference between the UWB sub-bands, since adjacent sub-bands are used.

III. Propagation Model of the Step-Index Multimode Fiber

In this section, the mathematical theory of the propagation model of the step-index multimode fiber is presented and discussed.

A. Modal field theory

As it was mentioned in Chapter 1, due to its high core-size, multimode fibers can support more than one propagation mode. This happens because the light inside the multimode fiber travels through several different paths, which means that some rays will travel faster than others. This effect is known by intermodal or modal dispersion

[10]. Another effect that has a significant impact on the multimode fiber propagation is the chromatic dispersion. This type of dispersion happens due to the different wavelengths that travel in the fiber have different propagation velocities [10]. In this work, only the impact of the modal dispersion is considered and studied.

Like all electromagnetic phenomena, the propagation of optical fields in multimode fiber is ruled by the Maxwell equations. The cylindrical symmetry of the optical fibers suggests the adoption of a cylindrical polar coordinate system to represent the spatial dependence of each Cartesian field component, as it can be seen in Figure 11.

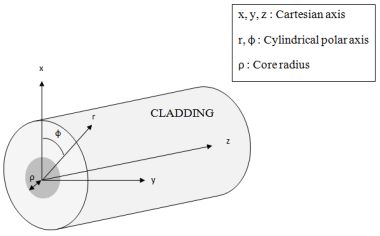

Fig. 11: Representation of the two coordinates systems used to represent the electric and magnetic fields in the multimode fiber.

Expressing the spatial dependence of each Cartesian field component in the cylindrical polar coordinate system (r, ϕ, z) makes possible to determined each modal field as a function of the radial and azimuthal coordinates.

According to Snyder and Love [11], the wave equation for the step-index fiber presented in Equation 6 [12]:

$$\{{\nabla_t}^2 + n^2k^2 - {\beta_{lm}}^2\}\Psi_{lm}(r,\phi) = 0 \tag{6}$$

where $\Psi_{lm}(r,\phi)$ corresponds to solutions of the scalar wave equation of the electric or magnetic field of each mode. Where ${\nabla_t}^2$ represents the Laplacian vector, n represents the refractive-index profile, β_{lm} represents the propagation constant and $k = 2\pi/\lambda$ represents the free-space wavenumber and λ represents the wavelength . Equation 7 shows the normalized transversal frequencies in the core and cladding region of each propagated mode, respectively:

$$\begin{cases} U_{lm} = \rho\sqrt{k^2n_{co}^2 - {\beta^2}_{lm}} \\ W_{lm} = \rho\sqrt{{\beta^2}_{lm} - k^2{n^2}_{clad}} \end{cases} \tag{7}$$

where ρ is the fiber core radius.

It is important to know that the sum of the squared values of the normalized transversal frequency in the core and in the cladding region is a constant for the modal solution of the optical fiber. This quantity is called normalized frequency or parameter *V* and is given by:

$$V \equiv \sqrt{U_{lm}^2 + W_{lm}^2} = \frac{2\pi\rho}{\lambda}\sqrt{n_{co}^2 - n_{clad}^2} \tag{8}$$

The normalized frequency V gives also information about the type of fiber used: for values of V between 0 and 2.405, the fiber propagates a single mode and for values superiors to 2.405 the fiber shows multimode operation [11].

According to Snyder and Love [11], the transversal normalized modal fields of the weakly guiding circular fibers are the ones presented in Table II:

TABLE II: Transversal modal fields of the weakly guiding step-profile multimode fiber.

Modal Field expressions		
$Mode$	$\mathbf{e}_{ti}$	$\mathbf{h}_{ti}$
$HE_{l+1,m}$	$\{\mathbf{x}cos(l\phi) - \mathbf{y}sin(l\phi)\}F_l$	$B\{\mathbf{x}sin(l\phi) + \mathbf{y}cos(l\phi)\}F_l$
$TM_{0,m}$	$\{\mathbf{x}cos(\phi) + \mathbf{y}sin(\phi)\}F_1$	$-B\{\mathbf{x}sin(\phi) - \mathbf{y}cos(\phi)\}F_1$
$TE_{0,m}$	$\{\mathbf{x}sin(\phi) - \mathbf{y}cos(\phi)\}F_1$	$B\{\mathbf{x}cos(\phi) + \mathbf{y}sin(\phi)\}F_l$
$EH_{l-1,m}$	$\{\mathbf{x}cos(l\phi) + \mathbf{y}sin(l\phi)\}F_l$	$-B\{\mathbf{x}sin(l\phi) - \mathbf{y}cos(l\phi)\}F_l$
$F_l = A\frac{J_l(UR)}{J_l(U)}$, $F_l = C\frac{K_l(WR)}{K_l(W)}$, $for\ l = 0,1,2,...$		$0 \leq \mathrm{R} \leq 1$, $1 \leq \mathrm{R} < \infty$
$B = n_{co}\sqrt{\frac{\varepsilon_0}{\mu_0}}$		

The characters *A* and *C* represent the integration constant pairs resulting from the solutions of the wave (or eigenvalue) equation [12]. These constants can be determined by specifying the boundary conditions at the fiber core-cladding interface, which require the continuity of the both electric and magnetic fields [12]. So, all the existing electric and magnetic fields must be equal at the radial coordinate $r = \rho$ or, equivalently, $R = 1$, which allows to determinate the unknown coefficients *A* and *C*. By applying the boundary conditions to the field expressions presented in Table II at the core-cladding interface $(R = 1)$, it is easy to conclude that:

$$A\frac{J_l(U)}{J_l(U)} = C\frac{K_l(W)}{K_l(W)} \tag{9}$$

$$\Leftrightarrow$$

$$A = C \tag{10}$$

In this work, the chosen values for the unknown integration coefficients are $A = C = 1$.

B. Mode classification

The number of allowed modes in the multimode fiber is given by the number of solutions of the Equation 6, for every existing azimuth mode number. Once the azimuth mode number is fixed, due to the smooth oscillatory behavior of the Bessel function of the first kind, a finite number of solutions is determined. It is clear from the mathematical structure of the modal solutions in Equation 6, that the azimuth mode number identifies the order of the Bessel functions in the core and cladding regions. So, all the modes characterized by the same azimuth mode number have the same Bessel order function. Another important statement is that the same value of the propagation constant can be common to different mode structures. This happens because for some different pairs of mode numbers, the eigenvalue equation has the same solution or, equivalently, the same propagation constant. This characteristic leads to mode degeneracy. The mode structures with the same propagation constants can be grouped and form the denominated *linearly polarized* (LP) mode groups [11]. In this work, the four types of allowed modes, namely HE, TE, TM and EH modes are considered separately.

1) TE_{0m} and TM_{0m} modes: As it was mentioned on the previous section, the TE_{0m} and TM_{0m} modes are obtained by setting $l = 1$ on the Equation 6. Since both $TE_{0,m}$ and $TM_{0,m}$ modes satisfies the same eigenvalue equation, they must necessarily have the same propagation constant for every fixed radial mode number m [12].

Substituting $l = 1$ on Equation 6 allows to determine the propagation constant of each $TE_{0,m}$ and $TM_{0,m}$ mode by solving numerically the following system [12]:

$$\begin{cases} U_{0m}\frac{J_0(U_{0m})}{J_1(U_{0m})} + W_{0m}\frac{K_0(W_{0m})}{K_1(W_{0m})} = 0 \\ U_{0m} = \rho\sqrt{k^2{n_{co}}^2 - {\beta_{0m}}^2} \\ W_{0m} = \rho\sqrt{{\beta_{0m}}^2 - k^2{n_{clad}}^2} \end{cases} \quad (11)$$

This system needs to be solved numerically. The only physical parameters envolved are the fiber core radius ρ, the refractive indexes n_{co} and n_{clad} and the operating wavelength λ. The physical multimode fiber parameters used in this dissertation are shown in Table III.

TABLE III: Parameters used for simulate a step-profile multimode fiber.

Fiber parameters	
Multimode fiber core radius [μm]	$\rho = 25$
Multimode fiber cladding radius [μm]	$\rho_c lad = 125$
Wavelength [nm]	$\lambda = 1550$
Core refractive index	$n_{co} = 1.48$
Cladding refractive index	$n_{clad} = 1.465$
Attenuation coefficient [dB/km]	$\alpha = 1.5$

The numerical solutions of the eigenvalue equation of the $TE_{0,m}$ and $TM_{0,m}$ modes, for the given set of the fiber parameters presented in Table III, are shown in Table IV.

TABLE IV: Computed eigenvalue for TE_{0m} and TM_{0m} modes.

TE_{0m}, TM_{0m} modes			
m	U_{0m}	W_{0m}	β_{0m} [$10^6 \mathrm{m}^{-1}$]
1	21.2671	1.1814	5.9388
2	18.5760	10.4220	5.9532
3	15.6611	14.4365	5.9666
4	12.6984	17.1007	5.9779
5	9.7103	18.9577	5.9868
6	6.0725	20.2178	5.9934
7	3.6627	20.9826	5.9976

2) $HE_{l+1,m}$ modes: The $HE_{l+1,m}$ modes are obtained by setting $l \geq 0$ in the Equation 6. The propagation constant of each $HE_{l+1,m}$ modes is determined by solving numerically the following system [12]:

$$\begin{cases} U_{l+1,m}\frac{J_{l+1}(U_{l+1,m})}{J_l(U_{l+1,m})} - W_{l+1,m}\frac{K_{l+1}(W_{l+1,m})}{K_l(W_{l+1,m})} = 0 \\ U_{l+1,m} = \rho\sqrt{k^2{n_{co}}^2 - {\beta_{l+1,m}}^2} \\ W_{l+1,m} = \rho\sqrt{{\beta_{l+1,m}}^2 - k^2{n_{clad}}^2} \end{cases} \quad (12)$$

In this case, the eigenvalue equation depends on the azimuth mode number. So, for each fixed azimuth number, the Equation 12 will present several solutions.

The eigenvalue equation has solutions until the azimuth mode number does not exceed the cut-off value. From that point on, there are no more intersections between the eigenequation members, which will lead to no more mode solutions for that mode family [12]. Figure 12 shows the situation of mode cut-off. In particular, for a fiber with the parameters presented in Table III, the mode $HE_{18,1}$ is still supported but the successive mode $HE_{19,1}$ is not, leading to no more mode solutions of the eigenvalue equation, which means that this mode can't be supported by the fiber used,

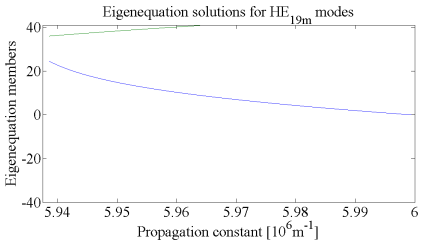

Fig. 12: Graphical solutions of the eigenvalue equation for HE_{19m} modes.In this situation, there is only one interception between the eigenequation members.

C. $EH_{l-1,m}$ modes

The $EH_{l-1,m}$ modes are obtained by setting $l > 1$ on the Equation 6. It is possible to determine the propagation constant of each $EH_{l-1,m}$ modes by solving numerically the following system [12]:

$$\begin{cases} U_{l-1,m}\frac{J_{l-1}(U_{l-1,m})}{J_l(U_{l-1,m})} + W_{l-1,m}\frac{K_{l-1}(W_{l-1,m})}{K_l(W_{l-1,m})} = 0 \\ U_{l-1,m} = \rho\sqrt{k^2{n_{co}}^2 - {\beta_{l-1,m}}^2} \\ W_{l-1,m} = \rho\sqrt{{\beta_{l-1,m}}^2 - k^2{n_{clad}}^2} \end{cases} \quad (13)$$

Like for the $HE_{l+1,m}$, the eigenvalue equation only has solutions until the azimuth mode number does not exceed the cut-off value. Figure 13 shows the situation of mode cut-off, for a fiber with the parameters presented in Table III. The $EH_{17,1}$ mode is no longer supported by this fiber, leading to no more mode solution of the eigenvalue equation, as it possible to see in Figure 13.

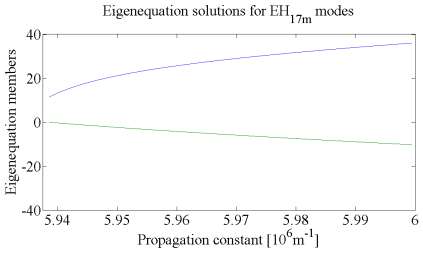

Fig. 13: Graphical solutions of the eigenvalue equation for EH_{17m} modes. There is no intersection between the eigenequation members, so this mode will never be sustained by the fiber used.

IV. Modal amplitude and modal power

The power generated by the electromagnetic fields of the optical fiber can be obtained from the Poynting vector. The Poynting vector represents the electromagnetic power flux density across the unit surface normal to the power flux direction [12]:

$$S \equiv \frac{1}{2}\mathrm{Re}\{\mathbf{E} \times \mathbf{H}^*\} \quad (14)$$

The modal power P_{lm} associated to each guided mode is given by the integration of the power flux density across the infinite fiber section A_∞ of that mode:

$$P_{lm} = \int_{A_\infty} S_{z,lm}(\rho,\phi)dA = \frac{1}{2}|a_{lm}|^2 \int_{A_\infty} \{\mathbf{E}_{t,lm}(\rho,\phi) \times \mathbf{H}^*_{t,lm}(\rho,\phi)\} \cdot \mathbf{z} dA \quad (15)$$

So, in order to determine the total power carried by the multimode fiber, it is necessary to determine the modal amplitudes a_{lm} of each guided mode. To achieve this purpose, the orthogonal property of the

bound mode set needs to be used. This property is derived from the Maxwell reciprocity theorem applied to a non-absorbing waveguide. The demonstration of this theorem is out of the scope of this work. A careful demonstration of this property can be seen in [11]. The modal amplitude of each guided mode under the weakly guiding approximation is given by Equation 16:

$$a_{l,m} = \frac{\int_{A_\infty} \{\mathbf{E}_s(\rho,\phi) \times \mathbf{z} \times \mathbf{E}^*_{t,lm}(\rho,\phi)\} \cdot \mathbf{z} dA}{\int_{A_\infty} |\mathbf{E}_{t,lm}(\rho,\phi)|^2 dA} \tag{16}$$

Equation 16 shows that once the source field $E_s(\rho,\phi)$ is known, the modal amplitude depends exclusively on the transversal component of the electric field. The total power carried by each mode, under the weakly guiding approximation, is given by:

$$P_{tot} = \frac{n_{co,clad}}{2Z_0} \sum_{l,m} \frac{|\int_{A_\infty} \{\mathbf{E}_s(\rho,\phi) \times \mathbf{z} \times \mathbf{E}^*_{t,lm}(\rho,\phi)\} \cdot \mathbf{z} dA|^2}{\int_{A_\infty} |\mathbf{E}_{t,lm}(\rho,\phi)|^2 dA} \tag{17}$$

1) Source field: At this point, it is important to define the optical source used in this work. The most common type of source used to couple the light into a multimode fiber is from a single mode fiber. The small SMF core radius, where the most of the optical fiber power is contained, allows launching the light in any point of the MMF region, exciting different types of modes. So, by choosing the point in the MMF where we want to couple the power launched from the SMF, it is possible to study the modal power distribution in the multimode fiber, because different launch conditions will excite different types of modes. A single mode fiber, in opposition to the multimode fiber, supports only one mode: the fundamental HE_{11} mode [1]. So, the field expression of the single mode fiber is similar the expression of the multimode fiber HE_{11} mode, presented in Table II.

TABLE V: Electromagnetic field of the single mode fiber.

Fundamental HE_{11} mode	
$\mathbf{e}_{ti}$	$\mathbf{h}_{ti}$
$\hat{\mathbf{x}}F_0$	$n_{smf,co}\sqrt{\frac{\varepsilon_0}{\mu_0}}\hat{\mathbf{y}}F_0$
$F_0 = A_{SMF}\frac{J_0(UR)}{J_0(U)}, \quad 0 \leq \mathrm{R} \leq 1$ $F_0 = A_{SMF}\frac{K_0(WR)}{K_0(W)}, \quad 1 \leq \mathrm{R} < \infty$	

where A_{SMF} represents the field amplitude coefficient and $n_{smf,co}$ represents the refractive index of the core region of the single mode fiber. Assuming the source is linearly polarized along the $\mathbf{x}$ axis, $\mathbf{E}_s(\rho,\phi) = E_s(\rho,\phi)\mathbf{x}$, the modal amplitude expression presented in Equation 16 can be simplified:

$$a_{l,m} = \frac{\int_{A_\infty} \mathbf{E}_s(\rho,\phi)\mathbf{E}^*_{x,lm}(\rho,\phi) dA}{\int_{A_\infty} |\mathbf{E}_{t,lm}(\rho,\phi)|^2 dA} \tag{18}$$

The next step is to determine the amplitude coefficient of the source electric field A_{SMF}. The amplitude coefficient can be obtained by manipulating the expression of the total power carried by the fiber P_{SMF} [13]:

$$P_{SMF} = \frac{1}{2}\int_0^{2\pi}\int_0^{\infty} (E_x {H_y}^* - E_y {H_x}^*) r dr d\phi \tag{19}$$

The total power carried by the SMF is obtained by summing the existing power in the core and cladding regions, $P_{SMF} = P_{co} + P_{clad}$. So, it is possible to split Equation 19 in two parcels, one representing the power contained in the core region and the other representing the power contained in the cladding region:

$$P_{co} = \frac{1}{2}\int_0^{2\pi}\int_0^{\rho} (E_x {H_y}^* - E_y {H_x}^*) r dr d\phi \tag{20}$$

$$P_{clad} = \frac{1}{2}\int_0^{2\pi}\int_{\rho}^{\infty} (E_x {H_y}^* - E_y {H_x}^*) r dr d\phi \tag{21}$$

By manipulating and summing the power in the core and cladding regions and solving the equation in order to A_{SMF}, the amplitude coefficient of the SMF field is obtained:

$$A_{SMF} = \sqrt{\frac{2P_{SMF}\frac{1}{\rho^2\pi}\sqrt{\frac{\mu_0}{\varepsilon_0}}}{\left\{n_{smf,co}\left(1+\frac{J_1^2(U)}{J_0^2(U)}\right) + n_{smf,clad}\left(\frac{K_1^2(W)}{K_0^2(W)} - 1\right)\right\}}} \tag{22}$$

So, it is obvious from Equation 19 that, by imposing the power transmitted by the electric source field, it is possible to determine the amplitude coefficient of the SMF field A_{SMF}. The physical parameters of the single mode fiber used in this work are presented in Table VI.

TABLE VI: Parameters used for simulate a step-profile single mode fiber.

SMF Fiber parameters	
Single mode fiber core radius [μm]	$\rho_{smf,co} = 4$
Single mode fiber cladding radius [μm]	$\rho_{smf,clad} = 125$
Wavelength [nm]	$\lambda = 1550$
Core refractive index	$n_{smf,co} = 1.48$
Cladding refractive index	$n_{smf,clad} = 1.477$

A. Multimode fiber transfer function

The multimode fiber transfer function can be represented as linear combination of the individual mode contributions. Each excited mode presents a fraction of the total launched optical power, associated with a given modal delay. The modal delay is defined by the product between the delay per unit length and the fiber length. The delay per unit length of each mode is given by the following expression [12]:

$$\tau_{lm} = \frac{\lambda}{2\pi c}\beta_{lm} \tag{23}$$

According to Bottacchi [12], the power transfer function of the multimode fiber is given by:

$$H_{MMF}(f) = \sum_{l,m} p_{lm} e^{-j2\pi f \tau_{lm} L_{MMF}} e^{-\alpha L_{MMF}} \tag{24}$$

where p_{lm} represents the fraction of power of each guided mode, f is transmission frequency, τ_{lm} represents the delay per unit length of each mode, L_{MMF} represents the length of fiber used and α represents the attenuation coefficient associated with the multimode fiber operating wavelength. In order to explore the power distribution of the different modes supported by the MMF, two different launching conditions are analysed: centred and 20 μm offset. Figure 14 and Figure 15 show the multimode amplitude responses for two different launching conditions of the optical source: zero and 20 μm offset, for fiber lengths of 100 m and 500 m, respectively.

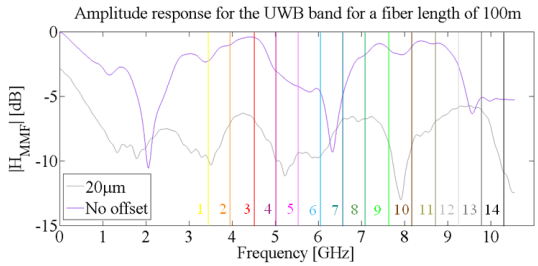

Fig. 14: Amplitude response for a fiber length of 100 m and for centred fiber axes and for a launch offset of 20 μm. The vertical colored lines represents the RF carrier frequency of each of the 14 UWB sub-bands.

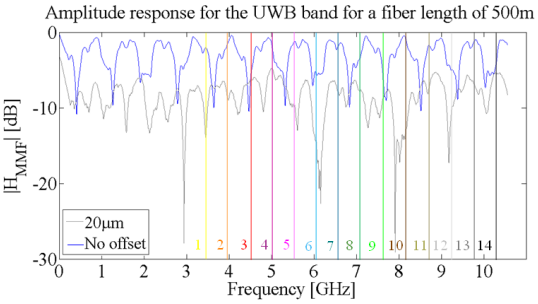

Fig. 15: Amplitude response for a fiber length of 500 m and for centred fiber axes and for a launch offset of 20 μm. The vertical colored lines represents the RF carrier frequency of each of the 14 UWB sub-bands.

The first important conclusion to take from the analysis of the amplitude frequency responses is that, for non-centred launching conditions of the source optical power, there is power coupling losses. These losses are due to the misalignment between the SMF and the MMF core axes. So, for an offset launching of 20 μm, there are coupling losses of 2.8 dB. From Figure 14 and Figure 15, it is possible to concluded that the multimode fiber frequency response is quite different from one sub-band to another. The RF carriers, which are located in a smoother region of the multimode fiber frequency response, will transmit information with better quality than the ones located in peak regions. Another important and expected result is that, the amplitude response of the multimode mode fiber has significantly smoother behavior for a fiber length of 100 m than for a fiber of 500 m. This happens because the length of the fiber has a direct impact on the modal delay which, consequently, affects the multimode fiber amplitude response, as it possible to see in Equation 24. The higher is the length of the fiber, the higher is the modal delay. This effect creates more distortion in the transfer function and leads to a significant degradation of the amplitude and delay responses. Another important feature of the multimode fiber propagation model is the modal power distribution. This distribution is strongly dependent on the launching conditions. Figure 16 presents the power fraction distribution for the existing fiber modes plotted as a function of its modal delay, for centred launching conditions. Figure 17, Figure 18, Figure 19 and Figure 20 show the power fraction distribution for the existing fiber modes plotted as function of its modal delay, for a 20 μm launch offset.

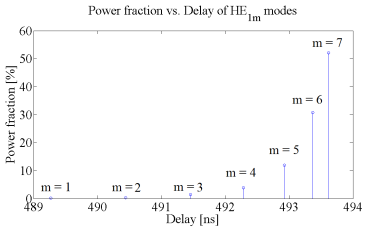

Fig. 16: Power fraction of the HE_{1m} modes for a fiber length of 100 m and centred launching conditions. In this situation, only the lower order HE_{1m} modes are excited.

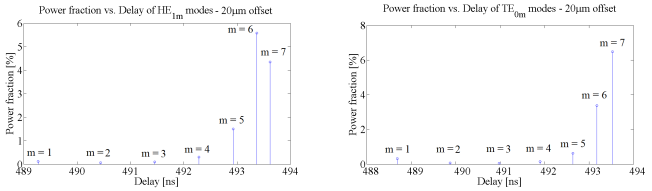

(a) HE_{1m} modes. (b) TE_{0m} modes.

Fig. 17: Power fraction of the HE_{1m} and TE_{0m} modes for a fiber length of 100 m and a launch offset of 20 μm.

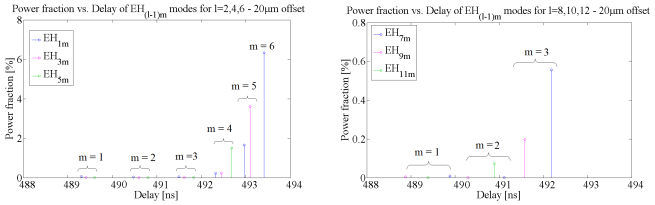

(a) EH_{1m}, EH_{3m} and EH_{5m} modes. (b) EH_{7m}, EH_{9m} and EH_{11m} modes.

Fig. 18: Power fraction of the $EH_{(l-1),m}$ modes for $l = 2, 4, 6, 8, 10, 12$, for a fiber length of 100 m and a launch offset of 20 μm.

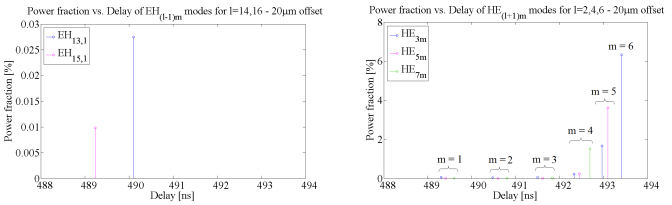

(a) EH_{13m} and EH_{15m} modes. (b) HE_{3m}, HE_{5m} and HE_{7m} modes.

Fig. 19: Power fraction of the $EH_{(l-1),m}$ modes for $l = 14, 16$ and $HE_{(l+1),m}$ modes for $l = 2, 4, 6$, for a fiber length of 100 m and a launch offset of 20 μm.

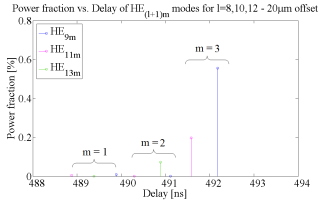

(a) HE_{9m}, HE_{11m} and HE_{13m} modes.

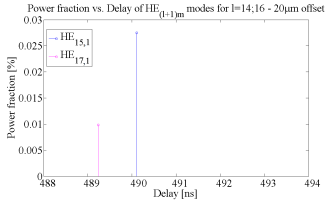

(b) HE_{15m} and HE_{17m} modes.

Fig. 20: Power fraction of the $HE_{(l+1),m}$ modes for $l = 8, 10, 12, 14, 16$, for a fiber length of 100 m and a launch offset of 20 μm.

An important feature of the modal power distribution in the multimode fiber is that, for each mode type, the modes with a higher modal delay, which are the ones with a higher value of the radial mode number m, have more power coupled than the lowest ones, for any launching conditions. This means that the higher modes within each mode type, carry more power, as it is possible to see, for example, in Figure 16 and 17.

Another important conclusion is that, for non-centred launching conditions, only the TE_{0m} and the odd $EH_{(l-1),m}$ and $HE_{(l+1),m}$ modes have coupled power.

V. OFDM-UWB SYSTEM PERFORMANCE

The maximum assessed distance will be limited by the degradation/distortion of the transmitted signal. The target bit error ratio of the system is 10^{-4}, since with this value it is possible to use effectively forward error correction (FEC) algorithms and improve the system performance. The bit error ratio of the system is determined by the semi-analytic gaussian approach [9]. The performance of the system for centred launching conditions is presented in Section V-A. In Section V-B, the performance of the system for a launch offset of 20 μm is presented.The numerical results obtained in this chapter are obtained for a launch power of 1 mW, for a Mach-Zehnder modulator with a modulation index of 10% and a V_{bias} point of 2.5 V and for Bessel filters of 6^{th} order with a -3 dB bandwidth of 400 MHz. The equalizer transfer function is obtained by a polynomial interpolation of 3^{rd} order.

A. Centred launching conditions

Figure 21 and Figure 22 show the performance of the system for the first and the fourth UWB sub-bands, respectively.

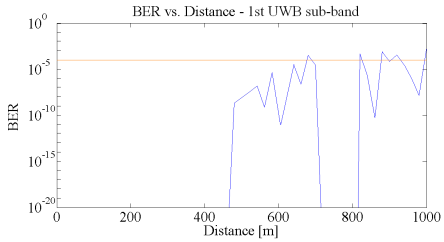

Fig. 21: Performance of the OFDM-UWB system for the first OFDM-UWB sub-band. The orange line represents the target bit error ratio of this system.

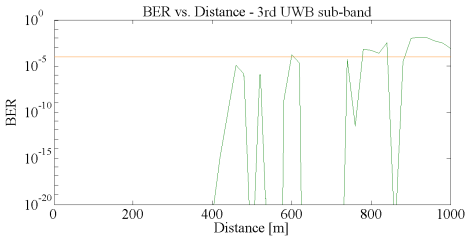

Fig. 22: Performance of the OFDM-UWB system for the third OFDM-UWB sub-band. The orange line represents the target bit error ratio of this system.

Figure 21 and Figure 22 show that the degradation of the signal is strongly dependent on the sub-band used and increases with the increase of the fiber length. This result is expected since the multimode fiber transfer function presents a different behavior for the different RF sub-carriers, as it is possible to see in Figure 14 and in Figure 15, in Chapter 3. The smoother is the behavior of the multimode fiber transfer function for the sub-band used, the better is the system performance. Figure 23 and Figure 24 show the received constellations without noise, in the third UWB sub-band, for fiber lengths of 100 m, 500 m and 600 m, respectively.

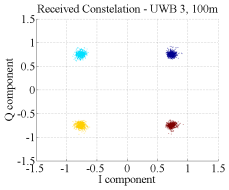

(a) Fiber length of 100 m.

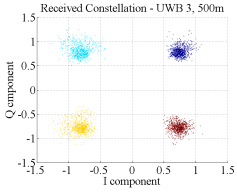

(b) Fiber length of 500 m.

Fig. 23: Received constellations for fiber lengths of 100 m and 500 m, in the third UWB sub-band.

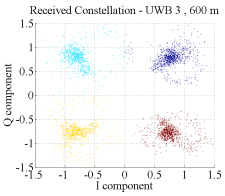

Fig. 24: Received constellations for a fiber length of 600 m, in the third UWB sub-band.

Analysing the results presented in Figure 24 and Figure 23, it can be concluded that the distortion of the received constellations increases with the increase of the fiber length. In fact, for a fiber length of 600 m, which is the situation close to the target bit error ratio, the received constellation presents a very high distortion. In this situation, the OFDM-UWB receiver is not able to decode the signal properly, since some of the received constellation points are spread all over the complex plan. So, the signal distortion limits the maximum assessed distance. So, for single-band transmission and centred launching conditions, the OFDM-UWB system is mainly limited by signal distortion and the maximum assessed distance is 560 m.

It is also be interesting to study the performance of the system in a multi-band environment. Figure 25 and Figure 26 show the

system performance when two and three OFDM-UWB sub-bands are transmitted simultaneously, respectively. The performance of the overall system is given by the performance of the worst sub-band.

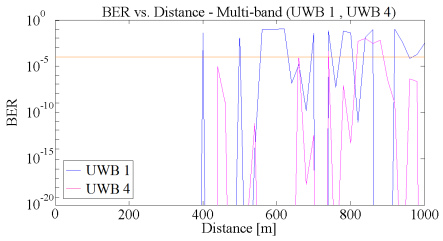

Fig. 25: Performance of the OFDM-UWB system for simultaneous transmission of the first and the fourth UWB sub-bands. The orange line represents the target bit error ratio of the system.

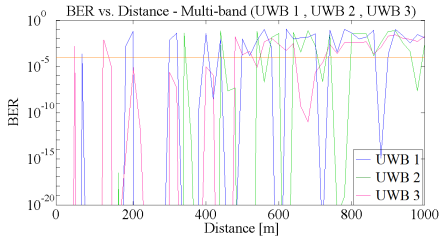

Fig. 26: Performance of the OFDM-UWB system for simultaneous transmission of the first, second and third UWB sub-bands. The orange line represents the target bit error ratio of the system.

Analysing Figure 25 and Figure 26, it is possible to see that the degradation of the system increases substantially when more than one sub-band is used simultaneously. For the case presented in Figure 25, the sub-band that presents the worst performance is the first one. In this situation, the maximum assessed distance which guarantees a BER inferior to 10^{-4} is 380 m, which is 180 m less than when only a sub-band is used. In the situation presented in Figure 26, the performance of the system decreases drastically. When three sub-bands are transmitting simultaneously, the maximum assessed distance is reduced to less than 50 m.

B. Launch offset of 20 μm

Figure 27 and Figure 28 present the bit error ratio of the first four UWB sub-bands, respectively.

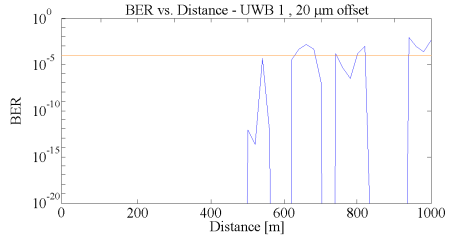

Fig. 27: Performance of the OFDM-UWB system of the first OFDM-UWB sub-band, for a launch offset of 20 μm. The orange line represents the target bit error ratio of this system.

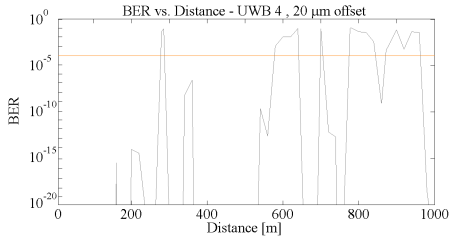

Fig. 28: Performance of the OFDM-UWB system of the fourth OFDM-UWB sub-band, for a launch offset of 20 μm. The orange line represents the target bit error ratio of this system.

Figure 28 and Figure 28 show that the degradation of the OFDM-UWB system for a launch offset of 20 μm is considerably higher than for centred launch conditions. As it was mentioned previous on the text, the performance of the overall system is limited by the performance of the worst sub-band. For a launch offset of 20 μm, the sub-band which presents a shorter distance for the target bit error rate (10^{-4}) is the fourth one. So, under this condition, the maximum assessed distance which guarantees a good performance of the OFDM-UWB system is about 270 m, less 330 m than for centred launching conditions.

Figure 29 and Figure 30 show the received constellations for the fourth UWB sub-band (which is the sub-band that limits the system performance), respectively, for fiber lengths of 100 m, 270 m and 300 m.

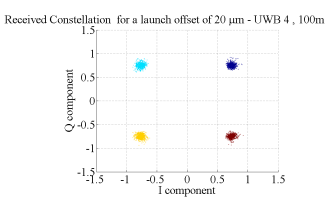

(a) Fiber length of 100 m.

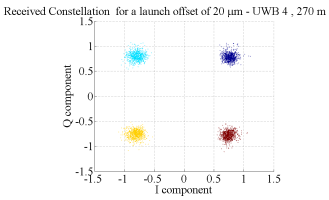

(b) Fiber length of 270 m.

Fig. 29: Received constellations of the fourth UWB sub-band for a launch offset of 20 μm, for fiber lengths of 100 m and 270 m.

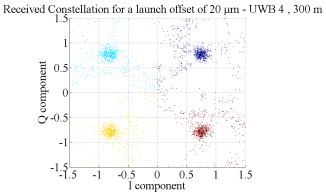

Fig. 30: Received constellations of the fourth UWB sub-band for a launch offset of 20 μm for fiber lengths of 300 m.

Figure 29 and Figure 30 show that, like for the centred launching conditions, when we have a launch offset of 20 μm, the increase of the fiber length also increases the distortion of the transmitted signal. The numerical results show that for fiber lengths exceeding 270 m, the received constellation presents a very high distortion, what makes not possible to demap the received constellation correctly.

So, for a launch offset of 20 μm, the maximum assessed distance is 270 m.

The use of a multi-band OFDM-UWB system will certainly have a strong impact on the BER of the overall system. Figure 31 and Figure 32 present the BER of the system for a launch offset of 20 μm, when two and three OFDM-UWB sub-bands are transmitted simultaneously, respectively.

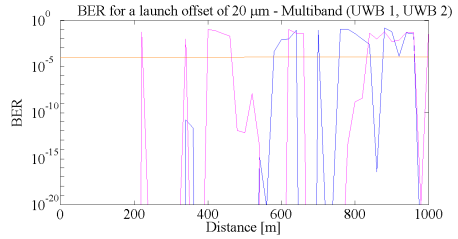

Fig. 31: Performance of the OFDM-UWB system for simultaneous transmission of the first and second UWB sub-bands, for a launch offset of 20 μm. The orange line represents the target bit error ratio of the system.

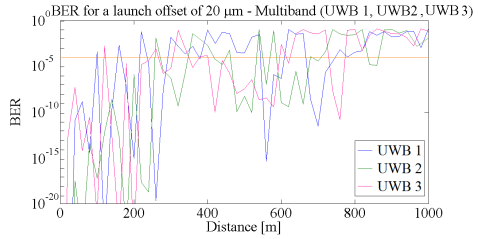

Fig. 32: Performance of the OFDM-UWB system for simultaneous transmission of the first, second and third UWB sub-band, for a launch offset of 20 μm. The orange line represents the target bit error ratio of the system.

As it was seen for the centred launching conditions, the use of the multi-band technique increases the degradation of the performance of the overall system. In the case of having two sub-bands transmitting simultaneously, the maximum transmission distance is slightly superior to 200 m. For the transmission of three sub-bands simultaneously, the maximum transmission distance is less than 100 m. Nevertheless, this value is superior to the centred launching conditions, for the same conditions.

VI. Conclusions

In this article, the transmission of OFDM-UWB signals along multimode fiber is studied and evaluated through a numerical simulation. The increasing capacity demands of the actual networks and the advantages of using multimode fiber optical systems are presented in section 1. In section 2, the main components of the OFDM-UWB system are presented and analysed. The system analysis in back-to-back configuration allowed to evaluate the performance of the system without multimode fiber transmission. The obtained results show that system performance depends on the number of sub-bands used. In section 3, the model of the multimode fiber propagation is developed from the theoretical model. The obtained results showed that the launching conditions, the fiber length and the carrier frequency of the UWB sub-band used have a significant impact on the multimode fiber transfer function. The excitation of higher order modes by setting non-centred launching conditions introduces coupling losses and contributes to the degradation of the multimode fiber transfer function. In section 4, the overall system performance is evaluated based on the bit error ratio, on the signal to noise ratio and on the received constellations. Three main conclusions are achieved: the launching conditions, the multimode fiber length and the number of UWB sub-bands used have a strong impact on the system performance. The maximum assessed distance for single-channel transmission and centred launching conditions is 560 m, while for a launch offset of 20 μm the maximum distance is only 270 m. In the case of having multi-band transmission of two sub-bands, for centred launching conditions the maximum transmission distance is 380 m and for a launch offset of 20 μm, the maximum transmission distance is 210 m. For the simultaneous transmission of the first three UWB sub-bands, the maximum transmission distance is less than 50 m, for centred launching conditions, and less than 100 m, for a launch offset of 20 μm. It was also concluded that the equalizer used in this simulator is not appropriated to the multimode fiber propagation, since it can't estimate correctly the channel's behavior between the pilots. A suggestion that will improve the system's performance is to use an equalizer more able to the channel's estimation between the pilots.

References

[1] R. Paschotta, "Encyclopedia of Laser Physics and Technology," *Wiley-VCH*, October 2008.

[2] F. 02-48, "Revision of Part 15 of the Commission Rules Regarding Ultra-Wideband Transmission Systems," *FCC*, April 2008.

[3] M. Benedetto and G. Giancola, "Understanding Ultra Wideband Radio Fundamentals," *Prentice Hall*, July 2004.

[4] R. T. M. M. J. A. Cartaxo and J. Marti, "Optical Distribution of OFDM and Impulse Radio UWB in FTTH Networks," *OFC/NFOEC*, 2008.

[5] J. Armstrong, "OFDM for Optical Communications," *J.Lightwave Technol. 27*, pp. 189–204, 2009.

[6] A. Photonics, "Modal launch conditions - measurement and control ," *on www.ardenphotonics.com/datasheets/wpmodcon.pdf*, June 2010.

[7] T. Alves and A. Cartaxo, "Performance Degradation Due to OFDM-UWB Radio Signal Transmission Along Dispersive Single-Mode Fiber," *IEEE Photonics Letters, vol.21, No.3*, pp. 158–160, February 2009.

[8] A. Cartaxo, "Transmissão por fibra optica," March 2005.

[9] T. Alves and A. Cartaxo, "Semi-analytical approach for performance evaluation of direct-detection OFDM optical communication systems ," *Optics Express, Vol. 17*, pp. 18 714–18 729, 2009.

[10] A. Cartaxo, "Transmissão em fibra óptica," *IST - folhas de apoio a disciplina de sistemas e redes de telecomunicacoes*, pp. 15–36, March 2005.

[11] A. Snyder and J. Love, "Optical Waveguide Theory," *Chapman and Hall, Ltd*, pp. 205–335, 1983.

[12] S. Bottacchi, "Multi-gigabit Transmission Over Multimode Optical Fiber: Theory and Design Methods for 10GbE Systems," *John Wiley & Sons, Inc.*, pp. 307–374, 2006.

[13] D.Marcuse, "Theory of Dielectric Optical Waveguides," *Academic Press, Inc*, pp. 60–82, 1991.